Ultrafast epitaxial growth of CuO nanowires using atmospheric pressure plasma with enhanced electrocatalytic and photocatalytic activities

Dey, A., Ghosh, P., Chandrabose, G., Damptey, L., Kuganathan, K., Sainio, S., Nordlund, D., Selvaraj, V., Chroneos, A., Braithwaite, N. S. J. & Krishnamurthy, S

DOI 10.1002/nano.202100191
ESSN 2688-4011

Publisher: Wiley Open Access

Received: 17 May 2021 | Revised: 21 June 2021 | Accepted: 16 July 2021

DOI: 10.1002/nano.202100191

RESEARCH ARTICLE

Nano Select Open Access WILEY

Ultrafast epitaxial growth of CuO nanowires using atmospheric pressure plasma with enhanced electrocatalytic and photocatalytic activities

Avishek Dey[1] | **Paheli Ghosh**[1] | **Gauthaman Chandrabose**[1] | **Lois A. O. Damptey**[1] | **Navaratnarajah Kuganathan**[2,3] | **Sami Sainio**[5] | **Dennis Nordlund**[5] | **Vimalnath Selvaraj**[6] | **Alexander Chroneos**[2,3] | **Nicholas St J. Braithwaite**[4] | **Satheesh Krishnamurthy**[1]

[1] School of Engineering and Innovation, The Open University, Milton Keynes MK76AA, UK

[2] Department of Materials, Imperial College London, London SW7 2AZ, UK

[3] Faculty of Engineering, Environment and Computing, Coventry University, Priory Street, Coventry CV1 5FB, UK

[4] School of Physical Sciences, The Open University, Milton Keynes MK76AA, UK

[5] SLAC National Accelerator Laboratory, Stanford Synchrotron Radiation Lightsource, Menlo Park, San Jose, California 94025, USA

[6] Department of Materials Science and Metallurgy, University of Cambridge, Cambridge CB3 0FS, UK

Correspondence
Satheesh Krishnamurthy, School of Engineering and Innovation, The Open University, Milton Keynes, MK76AA, UK.
Email: Satheesh.Krishnamurthy@open.ac.uk

Abstract

This work reports an environment friendly alternative to epitaxially grow copper oxide nanowires (NWs) on copper substrates using single step atmospheric pressure plasma jet assisted oxidation. NWs of average length 300 nm are grown rapidly in 5 minutes along with transforming the surface to superhydrophilic. This method introduces defects in the nanowire structure which is otherwise difficult to achieve due to the highly isotropic nature of nanowire growth. High resolution transmission electron microscopy reveals vacancies and structural defects such as lattice twinning and kinks. Theoretical investigations using density functional theory calculations indicated that oxygen vacancies reduces the adsorption energy of methanol molecules onto the CuO (111) surface and shifts the Fermi level towards conduction band. During electrocatalysis, these defect-rich nanowires exhibit twice the catalytic activity toward oxygen evolution reaction (OER) and methanol oxidation reaction (MOR) in comparison to the traditionally thermally grown nanowires. Moreover, retreating the electrodes after each stability test drops the contact resistance similar to the prisitine sample. Additionally, these NW photocathodes demonstrate an exceptional photocurrent of 2.2 $mAcm^{-2}$ and have an excellent degradation activity towards organic pollutants namely phenol and paracetamol. This facile growth method can be used to engineer nanowires of other transition metals with enhanced activities.

KEYWORDS

copper oxide, defect engineering, dye degradation, electrocatalysis, nanowire, photocatalysis methanol oxidation

1 | INTRODUCTION

Transition-metal oxides (TMOs) have attained considerable attention due to their low cost, good electrocatalytic properties and could be a suitable alternative to noble metals as electrode material for energy generation through catalytic applications.[1] Among the various TMOs there is accelerated interest in the nanostructured CuO for integration into various applications such as gas sensors, solar cells, field emission devices, photo-electrochemical processes, catalysis, batteries, supercapacitors and the likewise.[2–7] Direct conversion of methanol as fuel in Proton exchange membrane fuel cells (PEMFCs) holds enormous promise as a green source of energy.[8] Main advantages of electrocatalytic methanol oxidation in PEMFCs are low price, high theoretical energy density, good portability, and low toxicity.[8] Platinum-based electrocatalysts have been extensively used as the electrode material for methanol electrocatalysis. However, the high cost of Pt restricts its large implementation. There is a growing interest in several Cu based nanostructured oxides and model complexes have been reported as catalysts, including electro-catalysts and photo-catalysts.[9] Though CuO nanostructures are being investigated for various catalysis applications, still their prowess for MOR remains unexplored.

Factors influencing the electrochemical properties of the electrocatalyst materials are; structural morphology, surface energy, charge transfer kinetics, and surface-active sites.[10] 1 dimensional (1D) Nanowires (NW) are particularly desirable for electrocatalytic applications, due to their large surface areas.[11] Also, for a NW the mobility of the charge carries is much higher with respect to bulk due to decreased scattering along the length of the wire.[12,13] Thus, for catalysis, NWs are advantageous due to their large surface area resulting in increased adsorption of active molecules and the improved charge dynamics resulting in faster redox reactions.[14] Another factor that influences the electrochemical performance is the charge transfer efficiency from the active site of the catalyst to the corresponding current collector. Growing the electrocatalyst directly from the current collector is ideal to reduce the internal resistance and hence to sustain fast charge transfer between the catalyst site and the current collector during the redox reaction, with the added advantage of enhanced mechanical adhesion.[15] Recently, optimizing the reactivity of TMO based (Ni) catalytic sites via the introduction of oxygen defects has emerged as a novel route to improve the electrocatalytic activity of transition metal oxides.[16] The presence of oxygen vacancies found to increase the adsorption of reaction intermediates, in-turn enhancing electrochemical activity.[17] Oxygen vacancy induced enhanced activities have been reported for NiO, Co_3O_4, Fe_2O_3 and inorganic perovskites.[17–20] In this work, we present a design strategy for growth of CuO nanowires anodes supported by theoretical calculations, that can significantly improve their activity towards MOR. Here, we aim to incorporate these factors by growing CuO nanowires with abundant defects directly on to copper substrates.

Thermal oxidation is the most commonly used technique to synthesize copper oxide nanowires.[21,22] Other techniques include hydrothermal synthesis, electrochemical synthesis, thermal decomposition of copper salts and chemical de-alloying. [11,15,23] Plasma based oxidation has evolved as a highly efficient and clean technique to synthesize copper nanowires.[13] By using direct plasma oxidation using microwave plasma jet reactor, Kumar et al. demonstrated the with production of SnO_2, ZnO, TiO_2, and Al_2O_3 NWs.[24] Filipič et al. have carried out a thorough study on the growth dynamics of CuO nanowires grown in a low-pressure plasma environment operated at a radio frequency (RF) power of 150 W.[25–27] Altaweel et al. reported the growth of CuO NW using a microwave -after glow discharge at atmospheric pressure, but in a 2.45 GHz resonant cavity with 100 W RF power.[28] Notably, the major drawback of these techniques is that they require high power sources and specially designed chambers, making them unsuitable for large-scale production. Here we report a catalyst free synthesis of CuO nanowires using an atmospheric pressure plasma micro jet (μAPPJ) operated at 10 W, the lowest reported until now and is independent of any enclosed environment. APPJs are of significant practical importance because the plasma jets are not restricted within the dimensions of the electrodes and can be directed towards substrates.[29,30] APPJs are produced by passing a carrier gas typically He/Ar through an electric field applied between two electrodes. The plasma is blown out of the device in the form of a jet/plume by the flowing gas.[31] APPJ consists of abundant charged particles, radicals, neutral,metastable species along with radiations in the UV and visible regions that can be used to induce finite structural and electronic disorders in any substrate remotely.[32] Moreover, APPJ process/method is rapid, and it requires less than 5 minutes to grow nanowires of length greater than 300 nm, whereas it takes hours of thermal annealing to grow nanowires of similar lengths.[11] Successful implementation of this technique would lead to a large-scale roll-to-roll production of copper oxide nanowires, suitable for key industrial sectors such as electronics, optical and renewable energy. CuO NWs reported in this work show significantly enhanced electrocatalytic methanol oxidation in comparison to NWs grown via thermal annealing (400°C for 4 hours). The enhanced electrocatalytic activity is due to the formation of intrinsic defects in the form of oxygen vacancies in CuO structures. Combining density functional theory (DFT) calculations, surface sensitive X-ray photoelectron spectroscopy (XPS) and site

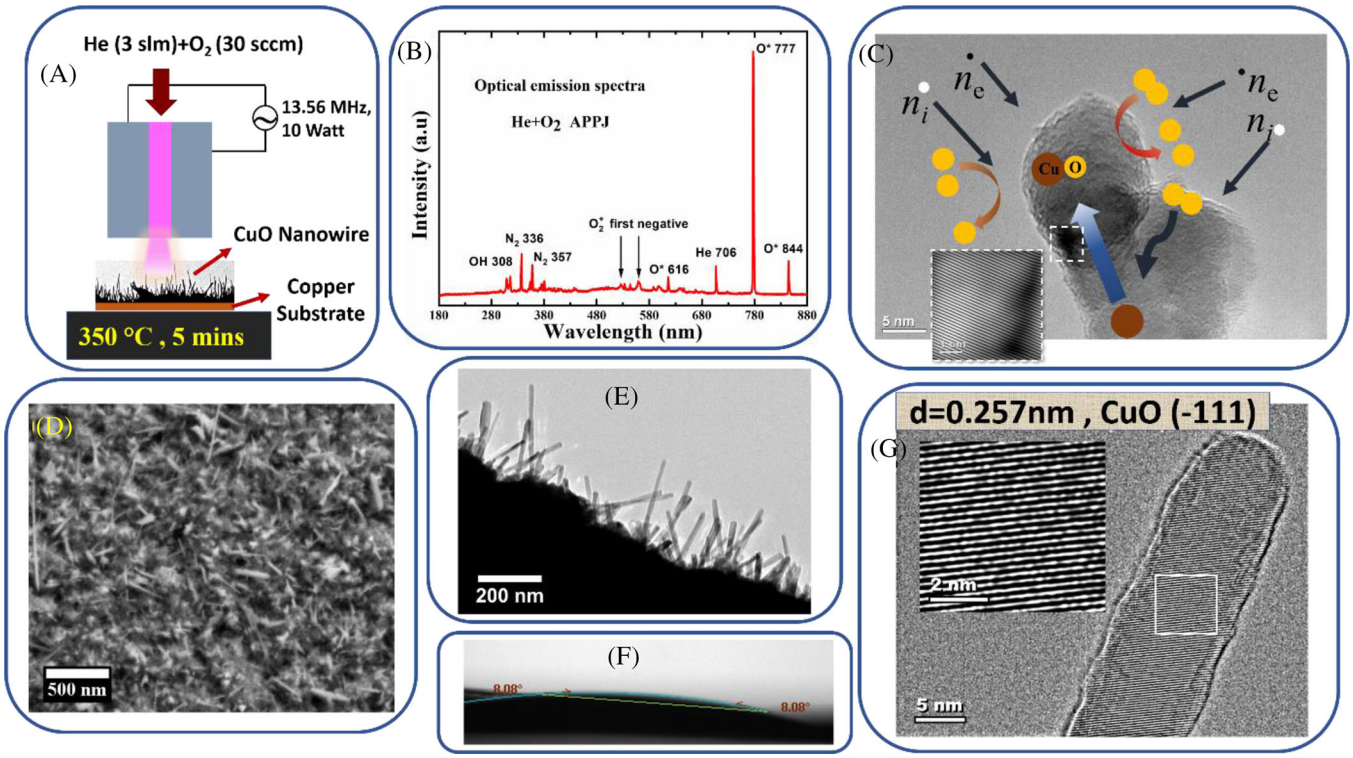

FIGURE 1 A, Schematic representation of the plasma functionalisation process. B, Optical emission spectra taken at the surface of the substrate; C, nucleation of the CuO nanowires under the influence of excited spieces in the plasma; D, SEM image of copper foil after 5 minutes of plasma functionalization, E, TEM image of the copper grid after 5 minutes of plasma functionalization; F, water contact angle of 5 minutes plasma treated copper foil; G, HRTEM image of a single crystal CuO nanowire with lattice orientation along (-111) direction

selective near edge x-ray absorption spectroscopy (NEXAFS) measurements, we have been able to gain deeper insight into the impact of oxygen vacancies on the MOR activity of CuO electrodes. Density functional theory together with dispersion correction (DFT+D) was used to simulate methanol (CH_3OH) molecule interacting with both stoichiometric and non-stoichiometric CuO (111) surface structures. The current simulation allowed us to comment on the relative ease of binding of CH_3OH molecule with and without defective surfaces. We have also demonstrated the reusability of the technique by three repeated MOR stability tests with intermediate plasma functionalisation between the stability tests. Additionally, the synthesised CuO NWs also demonstrated impressive activity as a cathode material towards photocatalytic hydrogen evolution reaction and photodegradation of organic pollutants.

The present work provides an innovative and sustainable route towards rational design of catalyst electrodes that could include sulphides, nitrides and other TMOs through defect engineering for applications ranging from fuel cells, electrolyzers, rechargeable metal-air batteries, CO_2 conversion and N_2 fixation.

2 | EXPERIMENTAL SECTION

2.1 | Synthesis of CuO nanowires

The experimental setup for growing copper nanowires on copper foils is shown schematically in Figure 1. To grow nanowires, the copper foil was placed on a hot plate, preheated to 350 ± 10°C and simultaneously exposed to the plasma jet for time varying from 1 to 5 minutes, with an interval of 1 minute. The radio frequency (RF) plasma jet used in this process is the same as described by Golda et al.[33] The plasma was ignited using a gas mixture of helium and oxygen, corresponding flow rates of 3 standard liters per minute (slm) and 30 standard cubic centimeters per minute (sccm), respectively, with an input power of 10 W. Distance between the jet and the copper substrate was maintained at 5 mm for all exposure times. For TEM analysis copper grids were also plasma treated at the same experimental conditions. Details of materials characterization and DFT calculations can be found in Supporting information.

2.2 | Electrochemical measurements

Electrochemical measurements were performed on Autolab PGSTAT M204 potentiostat/galvanostat equipped with a FRA32M module. The traditional three-electrode configuration consisting of Pt counter electrode, saturated calomel reference electrode (SCE), and CuO working electrode was used for all measurements. The substrates were attached with copper wires and covered with polypropylene tapes to obtain a square active area (1 cm x 1 cm) on the substrate. 1 M KOH (pH 14), 0.1 M KOH (pH 13) and pH 7 buffer electrolyte (HI-7007L, Hanna instruments) were used as electrolytes for OER measurements. 1 M KOH and 1 M methanol mixed in 3 to 1 ratio was used for MOR measurements. Both linear sweep voltammetry (LSV) and cyclic voltammetry were carried at a scan rate of 5 mV s^{-1}. Stability towards MOR was measured using chronoamperometry (CA) at a potential of 0.5 V versus SCE. Electrochemical impedance spectroscopy (EIS) was performed at an amplitude of 10 mV and frequency range of 0.1 Hz to 100 kHz. The activity of CuOp photocathodes were measured under chopped light (50 Hz) illumination of intensity equivalent to 1 Sun in 0.5 M Na_2SO_4 electrolyte. Also, degradation of organic pollutants like Mehylene Blue, Phenol and Paracetamol was used to gauge the photoactivity of CuOp for environmental remediation.

3 | RESULTS AND DISCUSSION

3.1 | Growth mechanism of CuO nanowires

CuO NWs were grown using atmospheric pressure plasma functionalization with helium and oxygen plasma jet on Cu substrates placed on a hot plate fixed at 350 ± 10°C(CuOp) (refer to Figure 1a). The processes were performed simultaneously to control the grain boundary diffusion in the plasma environment. The properties of this plasma grown NWs are compared to traditional CuO nanowires grown by annealing Cu foils at 400°C in a furnace, named CuOa. The morphology of the copper foil, before and after heating and simultaneous plasma-exposure was studied using (scanning electron microscopy) SEM shown in Figure S1. The substrates were subjected to the He+O_2 plasma jet for 1,2, 3, 4, 5 minutes to inspect the growth dynamics of CuO NWs. Figure 1 (d) and (e) shows the NWs grown on copper foil and transmission electron microscope (TEM) grids after 5 minutes of plasma functionalization, respectively. From Figure S1a, after plasma-exposure, the copper foil gets oxidized forming a thin oxide film. However, there is no growth of nanowires until after 2 minutes of exposure time (Figure S1b). But, the grains of CuO were distinctively observed. The nucleation sites or the seeding of the nanowires are observed after 3 minutes of plasma exposure as in Figure S1c. This shows that an optimal diffusion of oxygen is necessary to initiate the NW growth. The growth of nanowires becomes significant with the increase in treatment time from 3 to 5 minutes. The average length of the NWS after 5 minutes of plasma treatment were measured to be 300 ± 30 nm, which would have otherwise taken several hours of thermal annealing.[22] As comparison, the substrates were also exposed to the gas flow "plasma off" placed on a hot plate and no NWs were observed in this case as seen in Figure S2. This shows the efficacy of the atmospheric pressure plasma jet as a facile technique to grow copper oxide nanowires.

Two different mechanisms namely, (a) vapor-liquid-solid (VLS) and (b) vapor-solid (VS) have been widely used to describe growth of nanowires in the gas phase.[34,35] In our case, since the temperature involved is significantly lower than the melting point of copper and its oxides (1085 to 1326°C), these mechanisms cannot be considered for the growth of NWs in our case. The most plausible reason might be the gas phase diffusion of oxygen species from the plasma jet into the copper oxide lattice strained due to heat treatment. During thermal oxidation atmospheric oxygen dissociates on the surface of the copper substrates causing a slow growth of the oxide layer. The formation of nanowires is preceded by the formation of Cu_2O followed by the gradual oxidation to CuO.[21] Unlike the thermal process, the plasma jet-induced oxidation is a thermodynamically non-equilibrium process. Here, the reaction kinetics are accelerated by the energetic species present in the plasma. Optical emission spectra (Figure 1b) of the plasma jet shows the presence of excited atomic oxygen (O*) lines at 616, 777, and 844 nm and molecular oxygen ion (O_2^+) lines at 526 and 560 nm.[33] Here, nucleation of the nanowires is initiated by diffusion processes followed by growth due to recombination of the excited oxygen atoms at the surface. We have observed that the exposure of the substrates to plasma is not sufficient to oxidize the surface. As diffusion of oxygen is favored at higher temperatures (>300°C) F and occurs through the grain boundaries, an external source of energy was required. The electron backscatter diffraction (EBSD) images in Figure S3, shows the increase in grain size of the copper foil after NW growth. During the plasma based oxidation process metal ions moves from the core to the surface and the oxygen ions diffuse to the bulk. This diffusion slows down with the increase in oxide thickness. With the oxide layer on top of Cu foil, strain is developed at the interface. These internal stresses in the Cu foil are released as protuberance from the foil, and this is the stage when nucleation or seeding of the NWs starts as shown in Figure 1c and Figure S1c.[36] At this stage the NW grows

from the diffusion of Cu ions along bi-crystalline grain boundary from root to tip, where they react with adsorbed oxygen followed by surface diffusion towards the sidewall. This rather slow transfer of Cu ions can be accelerated by increasing the rate of oxygen adsorption. APPJs are known to enhance the surface adsorption and stabilization of oxygen radicals.[37,38] The abundance of oxygen radicals as observed in the OES spectra is critical for the rapid growth of NWs at high pressure. Also, the electrons in the plasma jet have sufficient energy to catalyze the dissociation or recombination of the oxygen molecules/ions on the NW surface. This results in oxidation of yet non-reacted copper ions. The heat released from the recombination to molecular oxygen can create a high temperature gradient at the NW tip, driving the accelerated surface diffusion of the adsorbed species. The transient electric field at the tip of plasma plume cannot be neglected as well. The rich dynamics of the plasma jet can provide favorable thermodynamic environment for single crystalline NW growth. Figure 1g shows one of the single-crystal NWs along the {111} lattice planes of the base CuO. The plethora of electrically charged particles, neutrals and radicals in APPJ provides a considerable advantage since they open a multitude of possibilities within a single environment, enabling higher efficiency to the NW growth process. Moreover, the ballistic effects of high energy ions at the surface generates a large number of defects such as vacancies, interstitial atoms and lattice distortions.[39] These defects are known to increase the activity of the electrocatalyst and will be discussed in the following sections. The activities of these plasma grown nanowires (CuOp) are compared with NWs grown through thermal annealing at 400°C for 4 hours named CuOa. To start with, the surface energy of CuOp and CuO(a) NWs show drastic difference in water contact angles. CuOp surfaces are superhydrophilic in nature with average water contact angles as low as 8° as shown in Figure 1f. It has been reported, the abundance of oxygen and hydroxyl radicals in the plasma jet transforms surfaces suitable for hydrogen bonding making them hydrophilic.[40] On the other hand, the average water contact angles of surface with thermally grown nanowires and copper foil are 140° and 93.55°, respectively (Figure S2). To achieve high efficiency in applications such as heat transfer, microfluidics, oil–water separation, photothermal conversion, catalysis and so on. require surfaces to be highly hydrophilic or super hydrophilic.[41–43] Due to its high thermal conductivity, copper is widely used as heat exchangers in hot water tanks, under floor heating systems, all weather football pitches and car radiators. The proposed technique to directly engineer Cu surfaces to become superhydrophilic in nature, will have an enormous impact for self-cleaning and antireflective coatings, antifogging films, thin-film devices, spray coating, heat transfer, separation membranes and smart surfaces with reversible switching abilities.[44]

3.2 | Characterization of the nanowires

The crystal structure and phases of these CuOp and CuOa nanostructures were investigated using X-ray diffraction (XRD) and Raman spectroscopy. Figure 2a shows the comparative XRD patterns of CuOa and CuOp. For CuOa there is a distinctive sharp peak at 38.5° corresponding to the (111) lattice of CuO (JCPDS No. 045–0937). While the other intense peaks at 43.5, 50.7 and 74.3° correspond to copper from the copper foil (JCPDS No. 04–0836).[45] For the plasma treated sample two additional peaks could be observed at 36.4 and 61.1° corresponding to the cubic Cu_2O phase (JCPDS No. 05–0667).[45] On comparing the two diffractograms no shift or broadening of the CuO features were observed between CuOa and CuOp, revealing that the monoclinic structure of CuO is preserved in the bulk. For CuOp, we attribute Cu_2O contribution might come from the remnant partially oxidized layer which acts as the building block for CuO NWs. This in turn suggests that 5 minutes is not enough time to convert all Cu_2O to the CuO. As the vibrational properties of these materials are dependent on their crystal symmetry. Hence, Raman spectroscopy a very sensitive to the phase changes of the material was studied. Raman Spectra for the CuOp and CuOa electrodes as shown in Figure 3b correlates well with the XRD results. Thermally grown NW electrodes show the presence of CuO phase only, characterized by the peaks at 297, 345, and 632 cm^{-1}. The peak at 297 cm^{-1} is attributed or assigned to the A_g mode, while the other two peaks correspond to the B_g phonon modes of the CuO crystal. In addition to CuO, the presence of the Cu_2O phase is reflected in CuOp samples by the presence of features at 148, 216, and 650 cm^{-1}. Modes related to the Cu_2O phase are noticeably sharper, this is due to the relative larger size of Cu_2O grains.[46,47] This also indicates that initially Cu oxidizes to Cu_2O, before eventually oxidizing to CuO.

In order to understand the surface chemistry of growth formation, X-ray photoelectron spectroscopy (XPS) was carried out on the treated and untreated copper foils. XPS is a powerful surface sensitive tool to probe the chemical and electronic properties at the very surface of the material, typically up to 5 nm.[30,48] Figure S4a shows the copper *2p* core level spectra for the oxidized and pristine copper foils. Cu 2*p* core level spectra of the as received copper substrate shows two sharp peaks around 932.5 ± 0.1 eV and 952.4 ± 0.1 eV corresponding to Cu $2p_{3/2}$ *and* Cu $2p_{1/2}$ peaks of metallic copper (Cu^0) with a negligible satellite peak between 940.0 to 945.0 eV. On the other hand, the oxidized foils show considerable broadening of the core

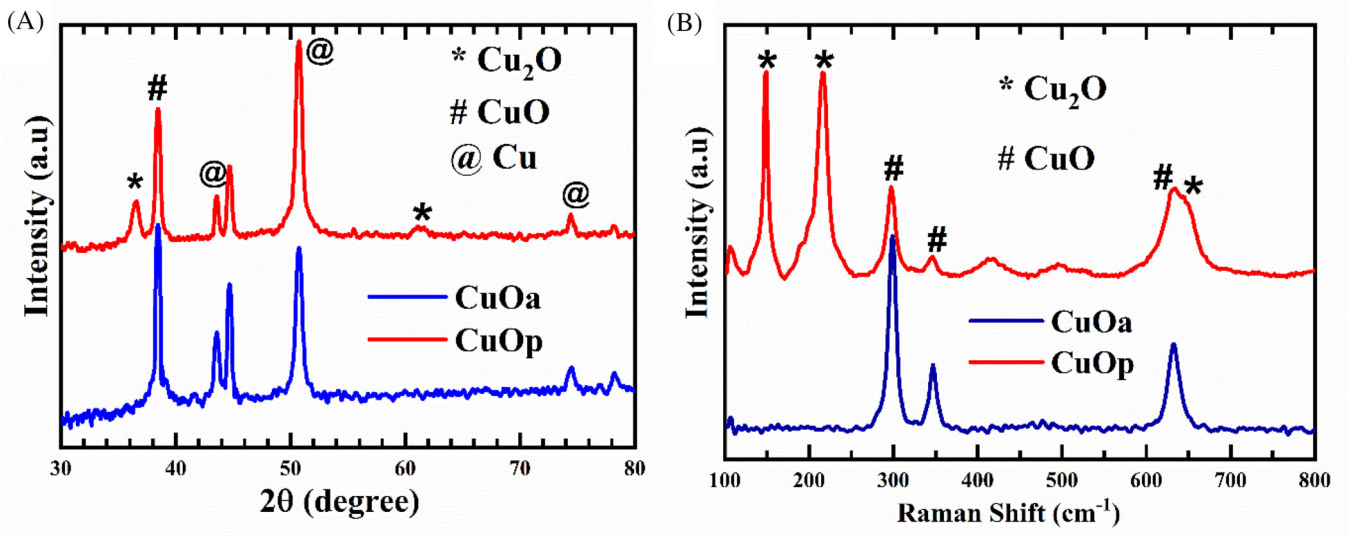

FIGURE 2 A, X-ray diffractograms of the copper foil annealed at 400°C for 4 hours (CuOa) and copper foil plasma functionalized at 400°C for 5 minutes (CuOp). B, Raman spectra of the same CuO samples

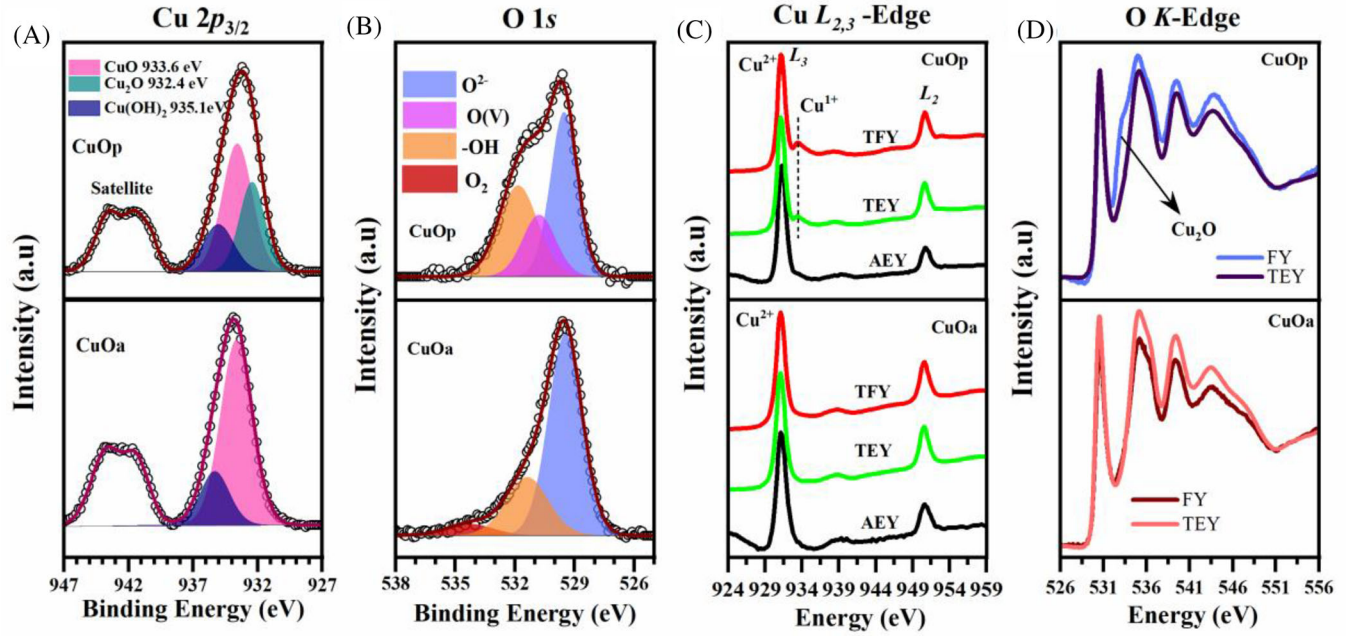

FIGURE 3 Comparison between (A) Cu $2p_{3/2}$ and (B) O 1*s* deconvoluted spectra for CuOp and CuOa NW electrode; C, Cu $L_{3,2}$-Edge absorption spectra; D, Oxygen *K*-Edge absorption spectra

levels and a prominent satellite feature. The broadening occurs due to the presence of multiple oxidation states of copper (Cu^{2+}, Cu^{1+}, Cu^0) after copper oxide formation.[49] Satellite peaks are the signature of ground state $3d^9$ configuration of divalent copper (Cu^{2+}). These satellite peaks originate due to the charge transfer of electrons from the O 2*p* to the Cu 3*d* orbital to screen the electric field of the core holes in the Cu 2*p* orbital created during the photoelectron emission process. The satellite feature for CuOp is weaker than CuOa, indicating to the lower O 2*p* to 3*d* charge transfer. This is attributed to the mixed valency of *d* orbitals (d^9/d^{10}) or perturbations at O 2*p* density of states caused by oxygen vacancy. The deconvoluted Cu $2p_{3/2}$ and O 1*s* spectra are shown in Figure 3. CuOp shows the presence of three oxidation states at 932.4 ± 0.2, 933.6 ± 0.2, and 935.1 ± 0.2 eV corresponding to Cu_2O, CuO and $Cu(OH)_2$, respectively.[49] While CuOa is predominantly in the Cu^{2+} state, as would be expected after 4 hours

of annealing in ambient and a high energy component around 935 ± 0.2 eV due to formation of surface copper hydroxide (reference).[49] The presence of Cu^{+} along with Cu^{2+} partially screens the Auger transitions shifting the auger peak to lower kinetic energies (refer to Figure S4b). Considerable changes were observed in the O1*s* line shapes between the CuOp and CuOa. The O 1*s* spectrum for CuOp deconvoluted into lattice oxygen O^{2-} (529.6 ± 0.2 eV), oxygen defects or vacancies (530.7 ± 0.2 eV) and contribution from hydroxyl groups OH^{-} (531.8 ± 0.2 eV).[17] The presence of an oxygen vacancy can affect the surrounding shell of the oxygen atoms by effectively altering their 1*s* binding energies and subsequent shells surrounding the vacancy. For CuOa the characteristic contribution from lattice oxygen dominates with lowered contribution from hydroxyl (531.8 ± 0.2) and adsorbed molecular components (534.2 ± 0.2). Creation of oxygen vacancies on the NW surface can facilitate the uptake of oxygen adsorbate and enhance the OH−adsorption, which can potentially be contributed to the improved OER activity. Moreover, oxygen vacancies have been found to annihilate the mobile holes that exist at O 2*p* level just above the valence band of CuO leading to the decrease of free hole concentrations. Hybrid density functional theory (DFT) calculations have found that the donor levels due to the oxygen vacancy are 1.7–2.3 eV above the valence-band maximum (VBM).[50] This phenomenon is evident from the shift the valence levels to higher binding energy shown in Figure S4c. The presence of oxygen vacancies have been reported elsewhere to enhance the electrocatalytic activities of NiO, CeO_2 and inorganic perovskites.[17,18,51]

X-ray absorption spectroscopy (NEXAFS) is a powerful tool to probe the electronic state of material was used. In NEXAFS, the empty/partially filled density of states is mapped by exciting the core level electrons the empty states following the dipole selection rule. These dipole allowed transitions render this technique highly sensitive to the local electronic structure, chemical configuration, oxidation state, molecular orientation and symmetry.[30] Figure 3c shows the normalized Cu $L_{3,2}$-edge spectra of CuOp and CuOa nanowires in Auger electron yield (AEY), total electron yield (TEY) and total flouroscence yield (TFY) modes. The corresponding surface sensitivities for this modes are 1-5 nm for AEY, 5-10 nm for TEY, and 50-100 nm for TFY.[52] Hence, information both from the surface and bulk can be acquired using XAS. Copper $L_{3,2}$-edge features results from from the dipole allowed $2p \rightarrow 3d$ transitions, where L_3 and L_2 corresponds to $2p_{3/2} \rightarrow 3d$ and $2p_{1/2} \rightarrow 3d$ absorptions, respectively.[47] Cu in CuO predominantly exists in $3d^9$ state and in Cu_2O exits as a combination of $3d^{10}$, $3d^9\ 4s^1$. For CuOa all the three modes have similar spectral feature. The intense absorption feature (L_3 edge) at 931.2 ± 0.2 eV, show surface and bulk are in Cu^{2+} state.[47] However, for CuOp NWs, an additional feature is observed both in TFY and TEY modes which is abscent in the AEY. This feature at 933.7 ± 0.2 eV corresponds to Cu^{1+} state.[47] Figure 3d presents the O *K*-edge absorption spectra in TFY and TEY modes. At the O *K*-edge of CuOa, there are four major peaks at 531.5 ± 0.2, 536.3 ± 0.2 eV, 540.4 ± 0.2 eV and 544.7 ± 0.2 eV and are in good agreement with the reported O-*K* edge spectra for CuO.[53] The sharp absorption peak at 531.5 ± 0.2 eV is assigned to O 2*p* hybridization with highly dispersive Cu 3*d* states of CuO while the higher energy peaks are form the hybridization O 2*p* with Cu 4*s* states of CuO.

Similar line shape of the TFY and TEY spectra indicate that CuO is the dominant phase both at bulk and at surface for CuOa. However, for CuOp and additional peak is observed at 533.1 ± 0.2 eV in the TFY mode, overlapping with the second major peak of CuO. This apparent broadening is due to the presence of Cu^{1+} in bulk. It has be reported that, for Cu_2O the O 2*p* to Cu 3*d* transition appear at an energy~ 2.6 eV higher energy than that of CuO.[53] Hence the absorption spectra for CuOp validates the coexistence of Cu^{1+} and Cu^{2+} for CuOp as depicted from XPS. The differences between the spectral features at O *K*-edge (TEY) for CuOp and CuOa is shown in Figure S4d. The $1s \rightarrow 3e_g$ transitions resulting from the hybridization of O-2*p* and Cu-3*d* states, and is observed to shift to higher energy for CuOp (Figure S4e). This shift originates form the oxygen vacancy induced electron doping.[54]

Transmission electron microscopy (TEM) was used to analyze the crystal structure and composition of the plasma synthesized nanowires. Figure 4a shows the TEM image of an individual plasma-grown nanowires with length >400 nm. Unlike thermally grown nanowires which tend to be tapered at the tip (shown in Figure S5), plasma grown nanowires were observed to have a uniform cross-section throughout their length with diameter ranging from 10 to 20 nm. As already shown in Figure 1g, some of the nanowires are highly oriented and single crystalline in nature. The single-crystalline NWs have followed the {111} lattice planes of the base CuO. This could be due to the thermal recrystallization of the NWs caused by the high-temperature gradient from ion bombardment or oxygen recombination. For CuO, the surface with (111) plane has lowest specific surface energy, which is the energetically favorable surface for nucleation and growth. The selected area diffraction pattern shows the presence of Cu_2O as well (refer to Figure S6). This could be emanating from the Cu_2O present in the oxidized copper substrate. It has been reported that depending on the oxygen partial pressure and temperature, oxygen vacancies can be incorporated during the ordering of the lattice.[55] Sun et al. determined that the CuO surface is not atomically flat but consists of high density of surface defects such as atomic steps, kinks,

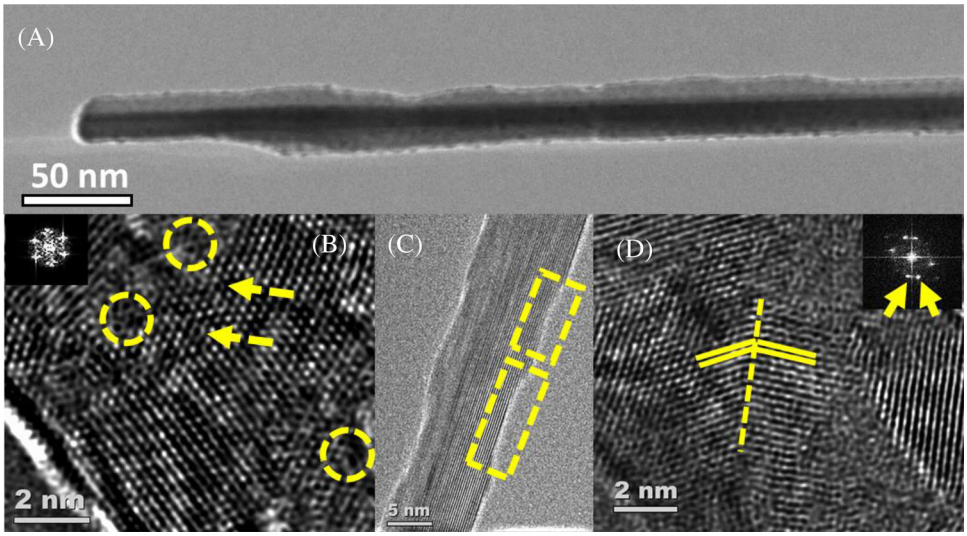

FIGURE 4 A, Transmission electron micrographs of CuO nanowires grown using plasma functionalization; B-D, High resolution images of different regions of NW highlighting the defects

ledges, and vacancies resulting from the surface growth of the CuO NWs both along the length and width of the nanowire.[55] The high-resolution images in Figure 4b-d highlights some of the defects in the lattice of CuO NWs. The inset of Figure 4b shows the diffuse streak diffraction patterns from the single crystal CuO NW. Four-fold diffraction spot streaks are observed along the ⟨111⟩ directions, which is an indication of the high defect densities in these nanowires on the {111} planes.[56] Voids in the lattice are highlighted in yellow circle showing the presence of vacancies. Figure 4c shows the steps at the edge of the nanowires, emanating from the ion induced etching. Additionally, twining defects are also observable in the NWs. The electron diffraction pattern obtained from twin domains can be seen as spot splitting along the ⟨111⟩ direction, as shown in Figure 4d. These unique structural features and their synergistic effect can manifest the enhanced performance towards electrochemical methanol oxidation.

3.3 | Electrocatalytic activity

The electrochemical activity of the plasma-synthesized CuO nanowires was then tested on a three-electrode configuration through a series of electrochemical measurements. In a typical electrochemical or photo-electrochemical water splitting process hydrogen evolution reaction (HER) occurs at the cathode while oxygen evolution reaction (OER) occurs at the anode.[29] OER is kinetically more sluggish involving four electron while HER is only a two electron-transfer reaction. To start with, CuOp catalysts were assessed based on their activity towards electrochemical water oxidation. Figure 5a-c shows the comparative polarization curves (non-*ir* corrected) of CuOp and CuOa in 1 M KOH, 0.1 M KOH and pH 7 buffer electrolyte, respectively. In all the polarization curves CuOp achieved higher current densities as compared to CuOa. This shows that the CuOp electrodes are catalytically more active. It is well known for CuO electrocatalysts that at high pH value the onset catalytic potential for OER becomes lower and the catalytic current density is greatly enhanced.[57] (as you say it's well-known provide reference) This is consistent with the shifts of potentials caused by the thermodynamics of H_2O adsorption during water oxidation.[57] Interestingly, the difference in onset potential between CuOp and CuOa increased with decreasing pH. Proving CuOp has faster charge transfer kinetics in electrolytes with low ionic concentration and large ohmic losses. We attribute this effect due to the presence of high density of oxygen vacancies and defects that act as active sites for adsorption during the catalytic processes. A similar increase in activity has previously been observed for plasma engraved Co_3O_4 catalysts towards OER.[19] Electrochemical impedance (EIS) shown in Figure 5d reveals the difference in charge transfer properties between the two NW electrodes at neutral pH. The charge transfer resistance (R_{ct}) is a critical parameter related to the OER process, determined by the diameter of the semicircle at high frequency region of the Nyquist Plot. The calculated R_{ct} at 0 V versus SCE, are 100 kΩ for CuOa and 31 kΩ for CuOp, indicating that the plasma synthesized NWs have almost three times lower charge transfer resistance for OER. This high affinity towards OH adsorption could be advantageous to increase the tolerance of the electrode against CO poisoning.

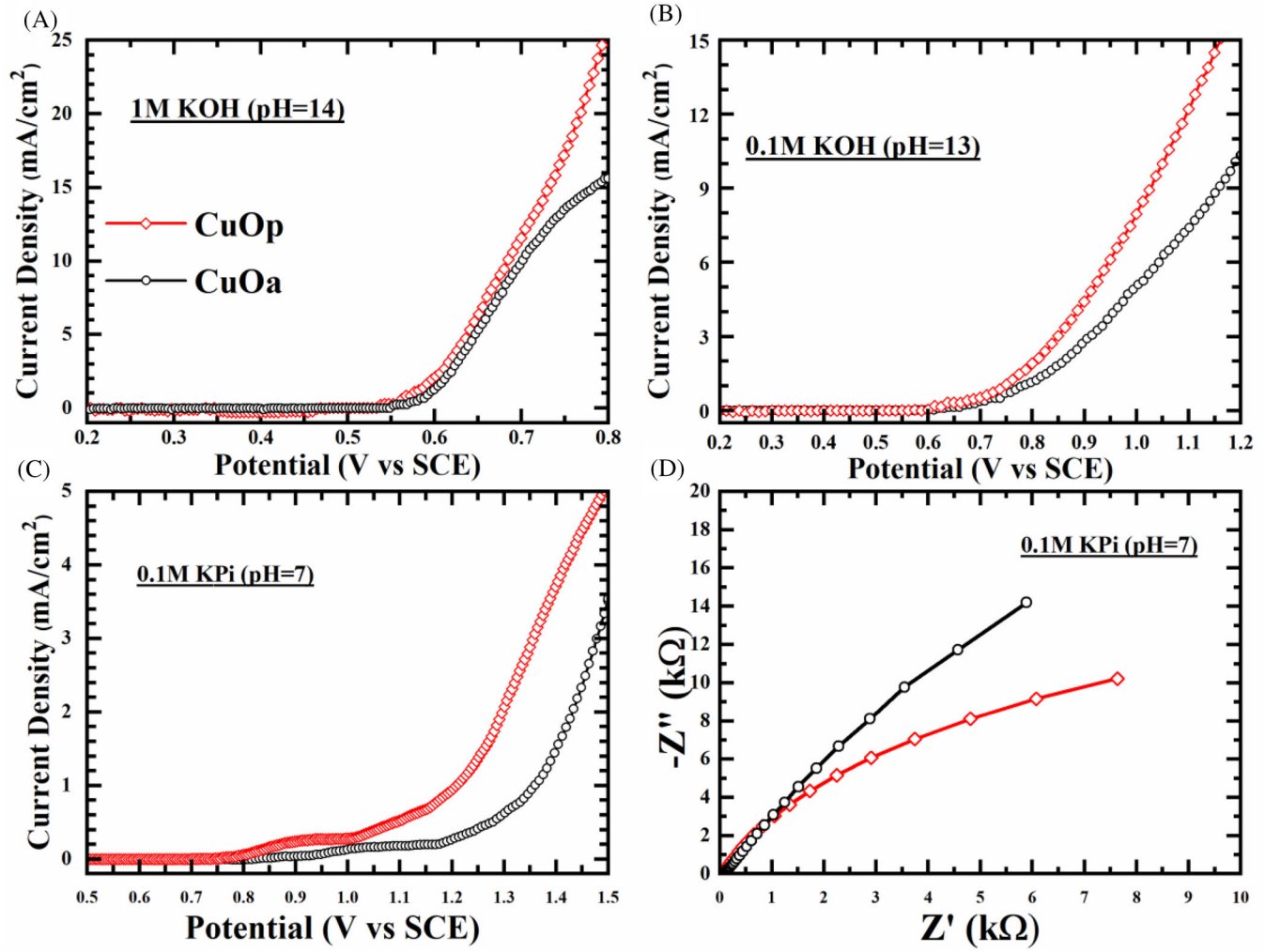

FIGURE 5 Electrochemical activity of CuOp and CuOa towards Oxygen evolution is studied using linear sweep in (A) 1 M KOH (pH 14); B, 0.1 M KOH (pH 13); C, 0.1 M KPi (pH 7); D) EIS in pH 7

The electrocatalytic activity of the NWs towards MOR is shown in Figure 6. Cyclic voltammetry (CV) and EIS illustrates the high activity of CuOp towards the MOR with respect to CuOa. Figure 6a shows the CV acquired in a potential window of 0 to 0.5 V versus SCE at scan rate of 5 mV s^{-1} in 1 M KOH+ 1 M CH_3OH (3:1 ratio). Before acquiring the measurements, CVs were carried out in a wide potential window at 50 mV s^{-1} until no variation in the CV curves were observed. Both the NW electrodes show a rise in anodic current at 0.5 V which is not present in the absence of methanol (shown in purple). CuOp electrode show a steep rise in the CV curve, achieving more than twice the current density (8.7 mA cm^{-2}) with respect to CuOa electrodes (4.2 mA cm^{-2}), but the onset potential for both the electrodes is the same. Pawar et al. reported anodic currents of ~10 mA cm^{-2} in 1 M KOH + 0.5 M CH_3OH electrolyte and onset potential of 0.42 V.[58] They used magnetron sputtered CuO thin films for MOR. The measured high current suggests that presence of defects at the electrode surface is responsible for faster charge transfer kinetics during the electrocatalytic oxidation of methanol. Furthermore, EIS in Figure 6b reveals that the defect-rich NWs have the lower interfacial charge-transfer resistance in comparison to the other two samples, supporting our claim of superior charge transport kinetics during the MOR process.

Stability of the CuOp electrode was tested by using chronoamperometry at 0.5 V versus SCE for 10,800 seconds in three steps of 3600 seconds as shown in Figure 6e. The second cycle between 3600 to 7200 seconds was carried with *iR*-compensation to test the electrode at higher anodic currents. CV curve for CuOp at 80% *iR* compensated condition is shown in Figure S7. During continuous MOR, intermediate carbonaceous species such as CO would begin to accumulate on the electrode surface thereby poisoning the catalyst.[59] Impedance spectra acquired after 3600 seconds of chronoamperometry at 0.5 V shows an increase in R_{ct} to 9 from 5 Ω. This CO contamination will impede

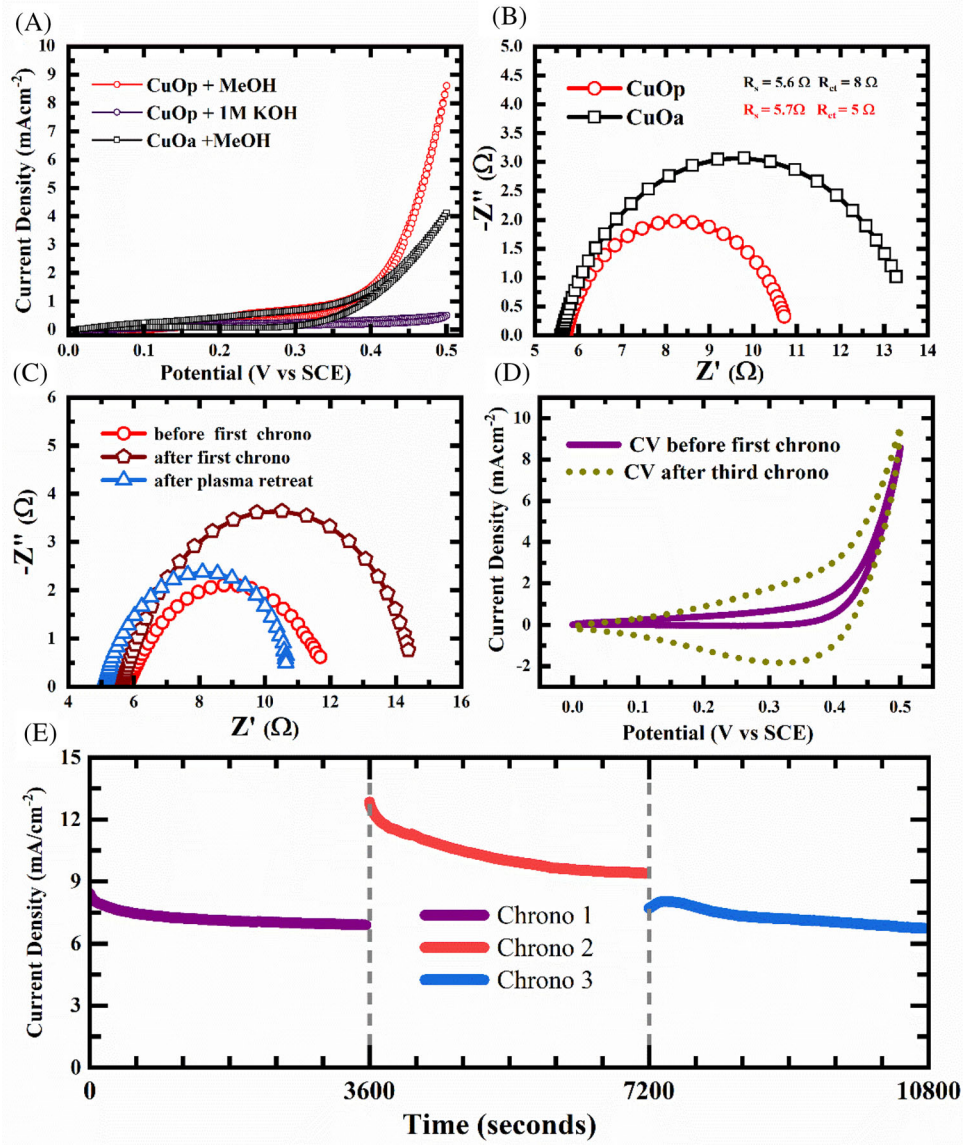

FIGURE 6 A) Cyclic voltammetry curves for NW electrodes with and without defects at a scan rate of 5 mV s^{-1}; B) electrochemical impedance spectra of these NW electrodes, C) Changes in impedance spectra of CuOp electrode after chronoamperometry of 3600 seconds and plasma cleaning, D) CV curves taken for fresh electrode and the same electrode when plasma treated after 10800 seconds of chronoamperometry test, E) Chronoamperometry tests of the CuOp electrodes at 0.5 V versus SCE. All measurements were carried out in 1 M KOH+1 M CH_3OH (3:1) electrolyte

the adsorption of OH, eventually reducing the catalyst activity. Here we observed a 20% drop in activity within 3600 seconds. Plasmas have traditionally been used as an effective, economic and environmental friendly technique for surface cleaning. Both the VUV radiation and oxygen ions present in plasma can dissociate most of the organic bonds.[32] To overcome the issue of contamination at the electrode surface, we retreated the electrodes using plasma after every 3600 seconds keeping all the conditions same as used during synthesis of the NWs. It was found that after the treatment R_{ct} dropped to 5.6 from 9 Ω, comparable to that of pristine sample (5 Ω). Even after the third cycle (10,800 seconds) of chronoamperometry, plasma treatment helped in retaining the activity of the electrodes towards MOR. This can be seen from the CV curves presented in Figure 6d. The observable increase in area of the CV curve could be related to the enhanced porosity of the electrode surface due to repeated cycling or increase in oxide layer thickness affecting the charge diffusion length.

3.4 | DFT calculation

In the previous section we established that CuO NWs with lattice defects and oxygen vacancies show enhanced

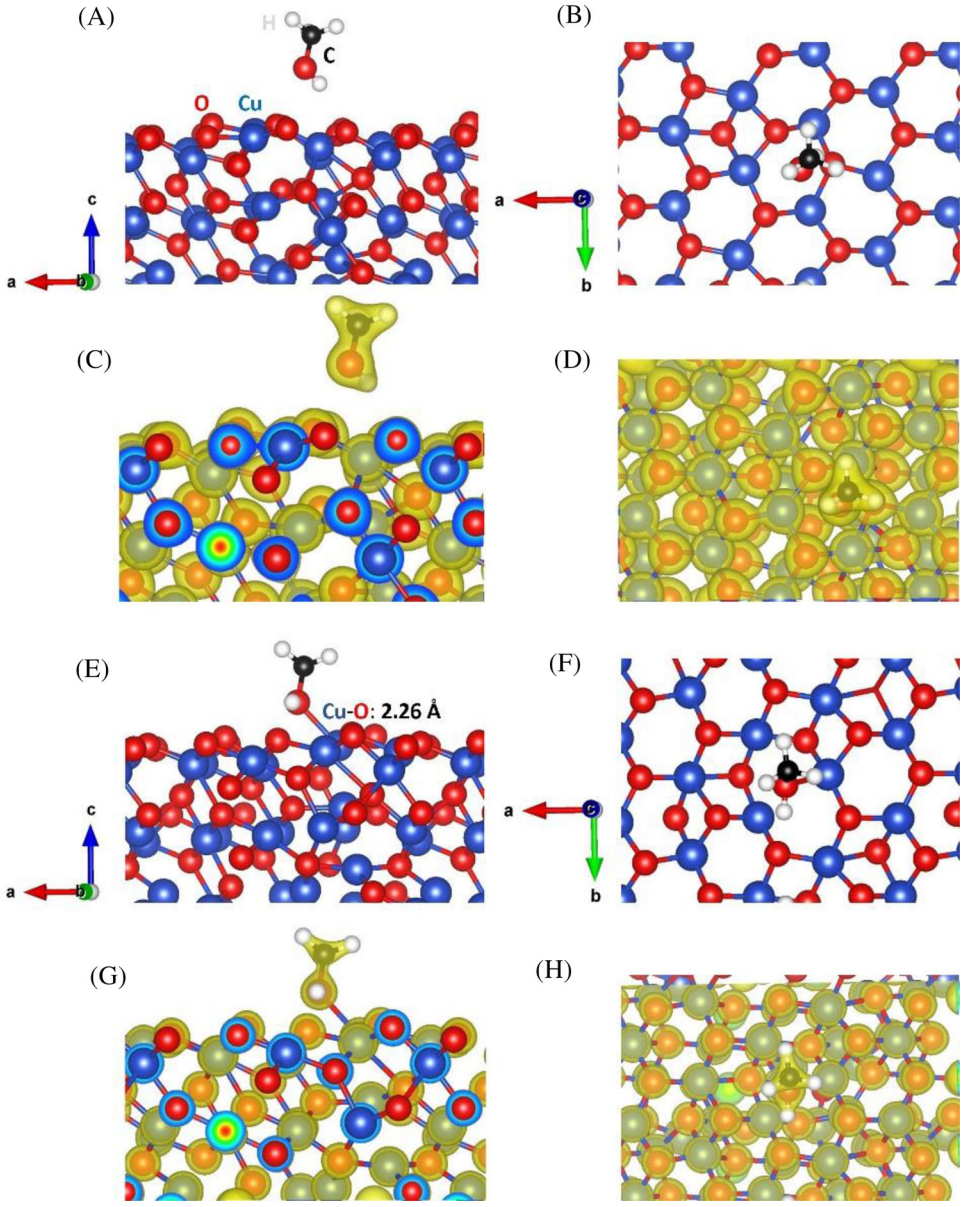

FIGURE 7 Relaxed structures of CH3OH bound to the CuO (111) surface (A) lateral and (B) top-views; corresponding charge density plots (C) and (D): Similar relaxed structures of CH3OH bound to the CuO (111) $V_O^{\bullet\bullet}$ surface (E) lateral and (F) side views; corresponding charge density plots (G) and (H). In all cases isosurface values was set to 0.20

activity towards MOR. To specifically understand the influence of oxygen vacancies on the catalytic property and electronic structure of CuO, density functional theory (DFT) calculations were carried out. To start with, energy minimization calculation was performed on the crystal structure to check the efficacy of the PAW pseudopotentials and plane wave basis sets used in this study. At room temperature, CuO crystallizes in the cubic phase [space group $Fm\bar{3}m$ (no. 225)].[60] The calculated lattice parameters and their corresponding experimental values are reported in Table S1. There is an excellent agreement between the calculation and the experiment showing the suitability of the parameters used in this study. A non-magnetic ground state was observed as reported by Himmetoglu et al. for the cubic phase of CuO using GGA functional.[61]

Now we start investigating the binding of CH_3OH on the perfect and defective CuO (111) surfaces. The perfect CuO (111) structure was constructed from the bulk cubic CuO and the defective structure was then created by removing an oxygen atom from the surface. The methanol molecule was then allowed to interact with the surfaces and the resultant complexes were allowed to relax. Optimized structures are shown in Figure 7. In the case of the perfect surface, the methanol molecule does not form any significant bonds with the surface atoms. However, the hydrogen atom of the O-H group in the CH_3OH molecule has a

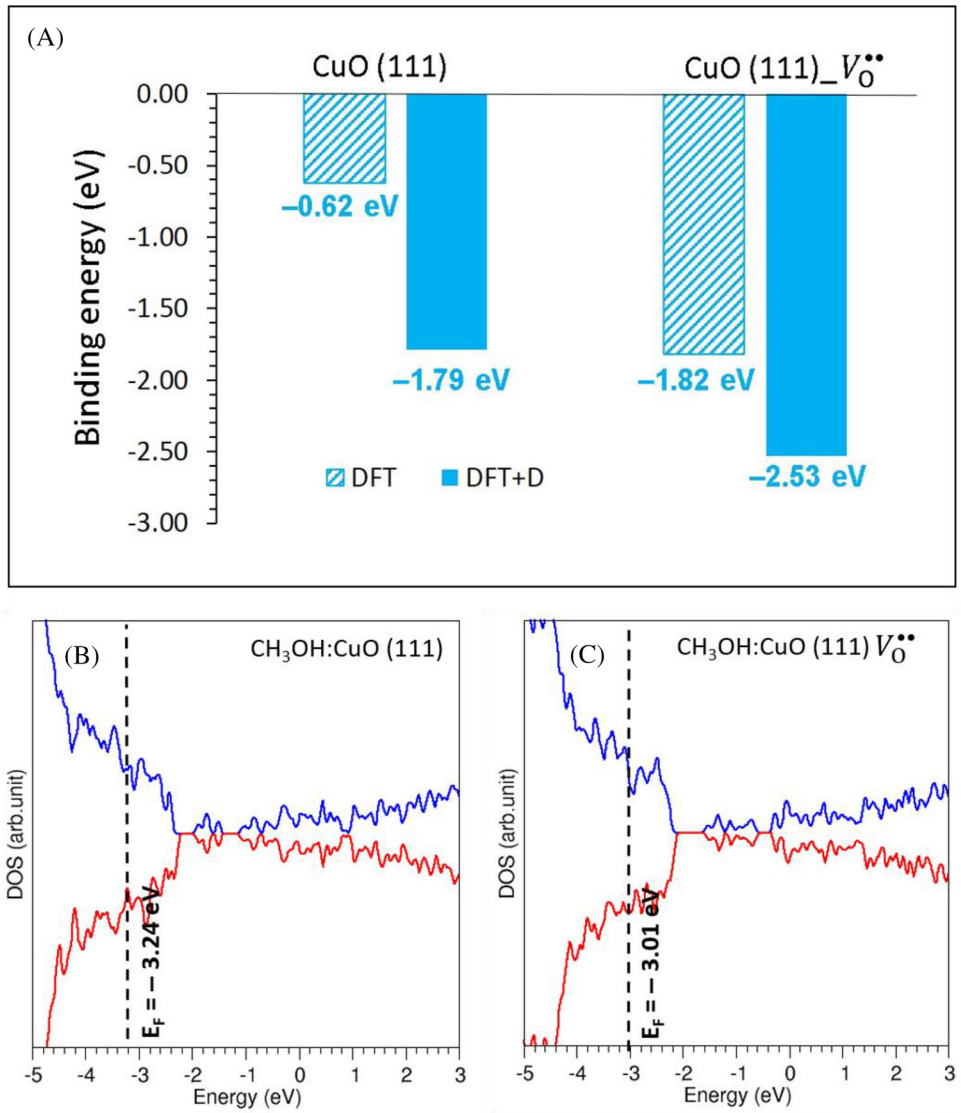

FIGURE 8 A, Binding energies of a CH_3OH molecule interacting perfect [CuO(111)] and defective [CuO (111) $V_O^{\bullet\bullet}$]. DFT and DFT+D denote binding energies calculated with and without dispersion correction, respectively. Total DOS plots for (B) CH_3OH:CuO (111) and (C) CH_3OH:CuO (111) $V_O^{\bullet\bullet}$. Black dot lines correspond to the Fermi level

non-bonding separation of 2.19 Å. The Cu atom on the defective surface has a bonding interaction with the oxygen of the O-H group in the CH_3OH molecule. The Cu-O bond distance is calculated to be 2.26 Å. The non-bonding interaction between the hydrogen of the O-H bond in the CH_3OH molecule and the oxygen in the surface is also noted. The non-bonding O-H separation is calculated to be 2.13 Å. The calculation shows that there is a stronger binding of the CH_3OH molecule with the defective surface. This is further confirmed by the calculated binding energies as shown in Figure 8a. Both perfect and defective surfaces exhibit exoergic binding energies of –0.62 and –1.82 eV, respectively calculated without dispersion meaning that the CH_3OH molecule is more stable with surfaces than its isolated gas phase. Once the dispersion is introduced the binding becomes stronger and their corresponding binding energies are calculated to be –1.79 and –2.53 eV, respectively.

The Bader charge analysis was carried out for all resultant complexes in order to estimate the charge transferred between the CH_3OH molecule and the surfaces.[62] Table 1 reports the amount of charge transferred and the net magnetic moment on the resultant complexes. The results show that in all cases only a small amount of electron is transferred from the CH_3OH molecule to the surfaces. The resultant complexes are magnetic except for CH_3OH: CuO (111) calculated without dispersion. It is clear that dispersion enhances the magnetic moments due to the strong

TABLE 1 Calculated charge transfer and magnetic moments in the resultant complexes formed between the CH3OH molecule and the surfaces

Structures	Charge transfer ($CH_3OH \rightarrow$ Surface) [e^-]		Magnetic moment [μ]	
	DFT	DFT+D	DFT	DFT+D
CH_3OH: CuO (111)	0.05	0.09	0.00	2.54
CH_3OH: CuO (111) $V_O^{\bullet\bullet}$	0.06	0.05	0.98	2.04

binding nature. Electronic structure calculations were performed on the bulk CuO and the surface structures. The cubic phase of CuO is reported to be metallic based on the calculations adopted with GGA functional (refer to Figure S8). The calculated density of states (DOS) plot for the CuO bulk is shown in Figure S8a. This is in agreement with the DOS reported by Himmetoglu et al.[61] Both perfect and defective surface structures are metallic. The removal of oxygen slightly shifts (by ~0.3 eV) the Fermi level towards the conduction band (refer to Figure 8 and Figure S8). There is a shift in the Fermi energy up on binding for both surfaces while maintaining the whole systems metallic.

3.5 | Photocatalytic activity

Being semiconductor in nature CuO NWs have applications in photocatalytic process. In this section we intend to evaluate the photocatalytic activity of the as-synthesized defect rich CuO NWs through photoelectrochemical (PEC) hydrogen evolution and photocatalytic degradation of methylene blue (MB). Figure 9a shows the PEC activity of CuOp photocathodes. Linear sweep voltammetry was conducted under chopped illumination (0.5 Hz) of intensity equivalent to 1 Sun in N_2 saturated 0.5 M Na_2SO_4 buffered at a pH of 6.8. The CuOp photocathodes showed a remarkable photocurrent of 2.2 mA cm^{-2} at 0 V versus RHE, which to our knowledge is the best for a bare CuO electrode. For a similar NW based photocathode prepared through thermal annealing the highest reported photocurrent is 1.4 mA cm^{-2} at 0 V versus RHE. Recently Li et al., found that after adding Pt as co-catalyst to the thermally-grown nanowires were able to achieve a maximum photocurrent of 1.6 mA cm^{-2}.[22]

The photodegradation of MB by CuOp in the presence of H_2O_2 was also used to benchmark the photoactivity of the defect rich NW catalyst and is recorded by UV-Visible absorption spectroscopy. Intensity of the signature absorbance peak of MB at ≈666 nm was used as the reference to measure the degradation rate Figure S9a. Hydrogen peroxide (H_2O_2) accelerates the photocatalytic activity of CuOp, by acting as a scavenger by releasing high energy $OH^{\bullet}$ species which degrades the organic dye molecules.[63] The reaction is initiated by the surface hydroxyl groups, observed in O 1*s* spectra (Figure 3b). Probable chemical reactions happening at the surface is mentioned in the Supporting Information. Reusable with repeatable activity is the main criteria for the successful implementation of a photocatalyst. However, CuO based catalyst suffer mostly due to photo-induced corrosion. Here, we addressed this issue by plasma treating the NW catalysts after each photocatalytic cycle. Figure 9b shows the repeatability of the MB degradation rate for three consecutive cycles. Noticeably, the sample without re-plasma treatment shows a decrease in dye degradation with an increase in number of photocatalytic cycle (refer to Figure S9). This can be due to photo corrosion of the NW surface or by adsorbed dye molecules blocking the incident light. Though the same overall dye removal efficiency of ≈97% is achieved in all three cycle, the inherent activity changed in each cycle. Figure 9c shows that the sample dye adsorption property increases by ≈30% after every plasma treatment. This increase in dye molecule adsorption is due two reasons, (i) increase in surface area (ii) increase in surface polarity from surface hydroxyl group.[64] Dye degradation rate constant (k) for all three cycles was calculated to be ≈0.025 min^{-1}, shown in Figure 9d. Table S2 compares the degradation activities of CuOp (current work) with the reported values. As our XPS, XRD and Raman measurements confirmed the presence of Cu_2O along with CuO. It is anticipated that the high photocatalytic activity arises from favorable band alignment between CuO and Cu_2O forming a type II heterostructure, which enhances the charge transfer and charge separation rate.[65]

Methylene Blue is widely reported as a model pollutant to measure the photodegradation potential of varioust catalysts, mainly due to the ease with which changes in concentration of MB can be monitored using UV-Vis Spectroscopy. However, it is to be noted that MB absorbs light in the visible range (550 to 750 nm). Since the incident illumination is mostly in the visible spectra, the influence of photo-absorption by the MB molecules cannot be excluded from the UV-Vis spectra used for evaluating the photocatalytic activity photocatalysts.[29] To overcome this challenge of visible light induced degradation, we have investigated the photocatalytic degradation of two organic pollutants namely phenol and paracetamol, both of these molecules have characteristic absorption peaks in the UV region.[29] Phenol is one of the leading cause of environmental hazard, as it is routinely found in industrial wastewaters.[66] Also, under the current circumstances there is a huge increase in the use of drugs like paracetamol as analgesic and antipyretic agent and pose a potential threat towards pharmaceutical contamination of aquatic

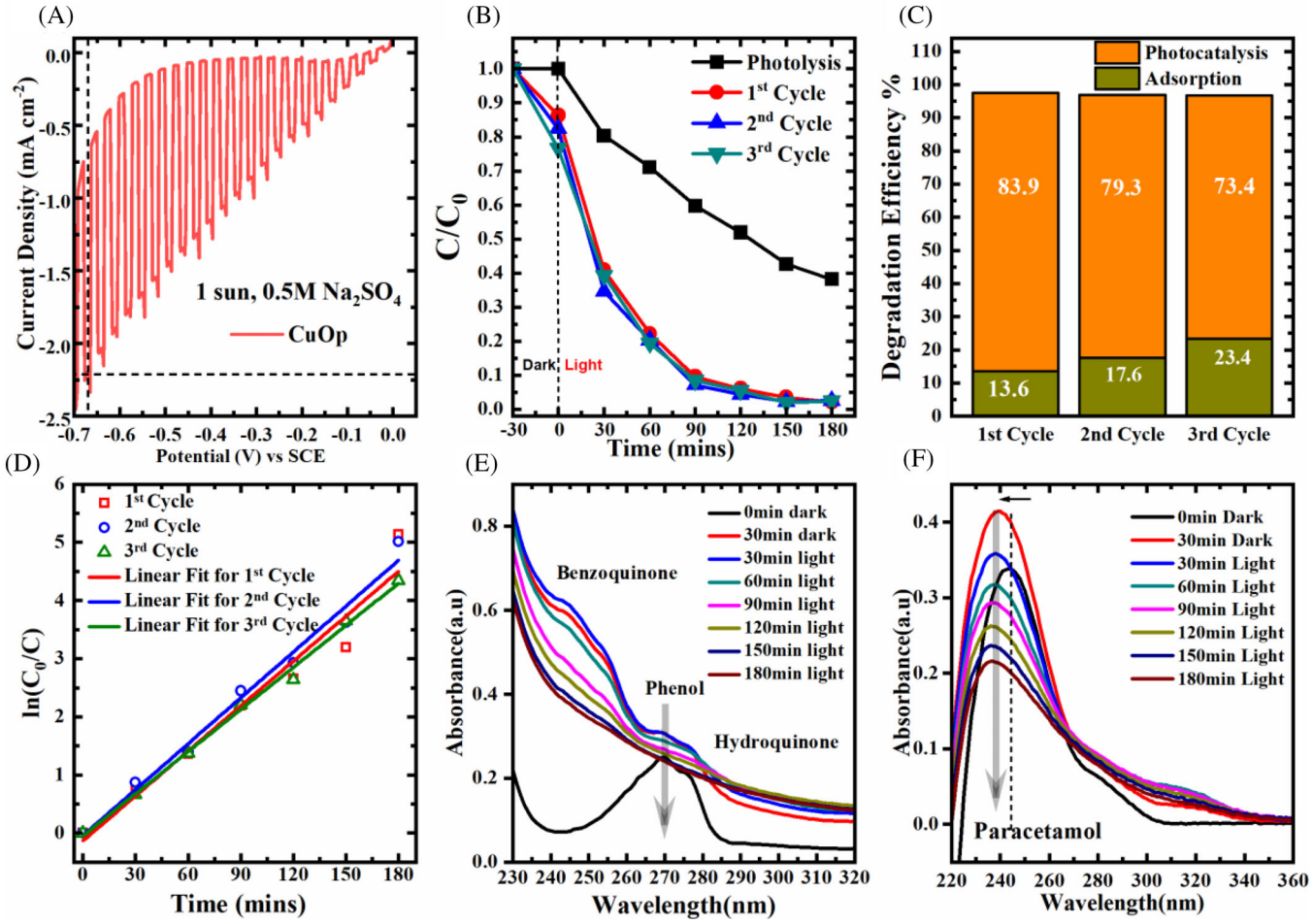

FIGURE 9 A, Photo electrocatalytic hydrogen evolution under 1 sun conditons by CuOp 0.5 M Na_2SO_4; B, adsorption and photocatalytic degradation of MB by the same CuOp sample for three consecutive cycle (plasma functionalized before each cycle); C, dye removal (adsorption and photocatalytic) efficiency (%) of CuOp sample; D, plot of photocatalytic degradation kinetics under light illuminated condition; UV–Vis absorption spectra for representing photocatalytic degradation of (E) Phenol and (F) Paracetamol

environments. Figure 9e presents the absorption spectra obtained at different intervals of the reaction solution containing phenol. The spectral features changed when the catalyst and H_2O_2 are added to phenol solution. The additional features are due to the conversion of phenol to p-benzoquinone (~ 240 nm) by the superoxide ($\bullet O_2^-$) radical and hydroquinone (~290 nm) by the hydroxyl radicals ($\bullet$OH).[29] This process is initiated by the spontaneous decay of H_2O_2 even in the dark conditions. After180 minutes of light, corresponding spectral features disappear giving a broad background from degraded products. This proves the degradation ability of CuOp towards phenol. Under illuminated conditions the photo-generated charge carriers at the surface of CuOp react with H_2O_2 producing hydroxyl and superoxide radicals. The presence of radicals in the reaction media escalates the breakdown of phenol via multi step ring opening reactions.[29] Paracetamol also known as 4-hydroxyacetanilide, 4-acetamidephenol or acetaminophen has a different degradation pathway with respect to phenol.[67] Figure 9f presents the absorption spectra of paracetamol solution collected at different reaction times. For paracetamol the characteristic absorption (λ_{max}) is observed at ~246 nm, originating from the n–π^* transition of C=O bonds.[68] After addition of scavenger (H_2O_2) the peak shows a hypsochromic shift of 7 nm, possibly due to oxidation of the parent molecule. After light irradiation the absorption band decreases in intensity. Upon extended photocatalysis an additional absorption peak at λ_{max} = 320 nm is observed which is characteristic of p-nitrophenol, one of the intermediate products of paracetamol degradation..[68]Eventually, intensity of the major peak at 240 nm decreases by 50% in 3 hours. For a thorough understanding of the photocatalytic activity of CuOp presented here, detailed spectroscopic and theoretical investigations are required. Importantly, from the results presented in this section, it is evident that plasma synthesized NWs could be a promising candidate for photocatalytic applications.

4 | CONCLUSION

In summary, we have successfully demonstrated a new APPJ assisted oxidation route to synthesize CuO NWs on copper substrates. The presence of ions, radicals and neutral species in the plasma are critical to the growth of these NWs. The state-of-the-art plasma jet used here operates at a minimal input power of 10 W. Through this process, NWs of length 300 ± 30 nm could be grown within 5 minutes, which would otherwise require several hours of thermal annealing to achieve. These NWs possess abundant defects as oxygen vacancies and lattice defects, which are introduced during the growth process. Interestingly, these defect rich NWs showed superior performance towards OER and MOR, in comparison to thermally grown nanowires. CuOp electrodes showed remarkable OER current density~80 mA cm^{-2} in 1 M KOH at 0.8 V versus SCE. During MOR, CuOp achieved more than twice the current density (8.7 mA cm^{-2}) with respect to CuOa electrodes (4.2 mA cm^{-2}) and showed a noticeable lower R_{ct} at 0.5 V versus SCE. The observed difference in activity is attributed to the presence of abundant defects on the NW surface. DFT calculations revealed that the presence of an oxygen vacancy considerably lowers the binding energy of methanol to CuO (111) surface, resulting in the significantly improved MOR kinetics. We have also demonstrated that a short duration plasma functionalization between cycles is an effective strategy to retain the activity and reuse the catalyst for prolonged operation. When used as photocathodes, the CuOp electrodes showed a remarkable photocurrent of ∼2.2 mA cm^{-2} at 0 V versus RHE under AM 1.5 G irradiation, 1.6 times the best value reported to date. We also have presented the potential of CuOp towards the degradation of organic pollutants. This work presents an efficient technique to engineer the catalytic property of CuO through defect engineering, which could be applied to design self-supported nanostructured electrodes of other catalytic materials.

ACKNOWLEDGMENTS

A.D. and S.K. acknowledges Recycling Lithium ion batteries for a sustainable technological and economic development (ReListed) DSTUKIERI-2018-19-008, Royal Society IES\R2\170272 Royal Academy of Engineering Newton Fund and European commission Smart innovative system for recycling wastewater project id: 958491 and creating closed loops in textile manufacturing industrial processes, Global challenges research fund on cleaning systems for solar cells.

CONFLICT OF INTEREST

The authors declare no conflict of interest.

DATA AVAILABILITY STATEMENT

Research data are not shared.

REFERENCES

1. S. Dou, X. Wang, S. Wang *Small Methods*. John Wiley and Sons Inc. **2019**, p 1800211.
2. D. P. Volanti, A. A. Felix, M. O. Orlandi, G. Whitfield, D. J. Yang, E. Longo, H. L. Tuller, J. A. Varela, *Adv. Funct. Mater.* **2013**, *23*(14), 1759.
3. H. M. Jeong, Y. Kwon, J. H. Won, Y. Lum, M. J. Cheng, K. H. Kim, M. Head-Gordon, J. K. Kang, *Adv. Energy Mater.* **2020**, *10*(10), 1.
4. H. Yang, Y. W. Hu, J. J Chen, M. S. Balogun, T. Jie, P. P. Fang, S. Zhang, J. Chen, Y. Tong *Adv. Energy Mater.* **2019**, *9*(27), 1901396.
5. S. Wu, W. Lv, T. Lei, Y. Han, X. Jian, M. Deng, G. Zhu, M. Liu, J. Xiong, J. H. Dickerson, W. He, *Adv. Energy Mater.* **2017**, *7*(14), 1700105.
6. L. Sun, Y. Zhuang, Y. Yuan, W. Zhan, X. J. Wang, X. Han, Y. Zhao *Adv. Energy Mater.* **2019**, *9*(48), 1902839.
7. C. Zhang, W. Lv, G. Zhou, Z. Huang, Y. Zhang, R. Lyu, H. Wu, Q. Yun, F. Kang, Q. H. Yang *Adv. Energy Mater.* **2018**, *8*(21), 1703404.
8. T. Zhang, Y. Sun, X. Li, X. Li, D. Liu, G. Liu, C. Li, H. J. Fan, Y. Li *Small Methods* **2020**, *4*(1), 1900709.
9. M. B. Gawande, A. Goswami, F.-X. X. Felpin, T. Asefa, X. Huang, R. Silva, X. Zou, R. Zboril, R. S. Varma *Chem. Rev.* **2016**, *116*(6), 3722.
10. M. Ma, K. Djanashvili, W. A. Smith *Angew. Chemie - Int. Ed.* **2016**, 6680.
11. G. Fritz-Popovski, F. Sosada-Ludwikowska, A. Köck, J. Keckes, G. A Maier. *Sci. Rep.* **2019**, *9*(1), 1.
12. Z. Zhang, R. Dua, L. Zhang, H. Zhu, H. Zhang, P. Wang *ACS Nano* **2013**, *7*(2), 1709.
13. G. Filipič, U. Cvelbar *Nanotechnology* **2012**, *23*(19), 194001.
14. G. Fu, X. Yan, Z. Cui, D. Sun, L. Xu, Y. Tang, J. B. Goodenough, J. M. Lee *Chem. Sci.* **2016**, *7*(8), 5414.
15. S. M. Pawar, B. S. Pawar, A. I. Inamdar, J. Kim, Y. Jo, S. Cho, S. S. Mali, C. K. Hong, J. Kwak, H. Kim, H. Im *Mater. Lett.* **2017**, *187*, 60.
16. J. Bao, X. Zhang, B. Fan, J. Zhang, M. Zhou, W. Yang, X. Hu, H. Wang, B. Pan, Y. Xie *Angew. Chemie - Int. Ed.* **2015**, *54*(25), 7399.
17. Y. Zhu, L. Zhang, B. Zhao, H. Chen, X. Liu, R. Zhao, X. Wang, J. Liu, Y. Chen, M. Liu *Adv. Funct. Mater.* **2019**, *29*(34), 1.
18. W. Yang, X. Yang, J. Jia, C. Hou, H. Gao, Y. Mao, C. Wang, J. Lin, X. Luo *Appl. Catal. B Environ.* **2019**, *244*(December 2018), 1096.
19. L. Xu, Q. Jiang, Z. Xiao, X. Li, J. Huo, S. Wang, L. Dai *Angew. Chemie - Int. Ed.* **2016**, *55*(17), 5277.
20. Q. Yang, J. Du, J. Li, Y. Wu, Y. Zhou, Y. Yang, D. Yang, H. He *ACS Appl. Mater. Interfaces* **2020**, *12*(10), 11625.
21. X. Jiang, T. Herricks, Y. Xia *Nano Lett.* **2002**, *2*(12), 1333.
22. J. Li, X. Jin, R. Li, Y. Zhao, X. Wang, X. Liu, H. Jiao *Appl. Catal. B Environ.* **2019**, *240*, 1.
23. A. S. Ethiraj, D. J. Kang *Nanoscale Res. Lett.* **2012**, *7*(1), 1.
24. Y. Kumar, J. H. Kim, C. Pendyala, B. Chernomordik, M. K. Sunkara *J. Phys. Chem. C* **2008**, *112*(46), 17750.
25. G. Filipič, O. Baranov, M. Mozetič, K. Ostrikov, U. Cvelbar *Phys. Plasmas* **2014**, *21*(11), 113506.
26. G. Filipič, O. Baranov, M. Mozetič, U. Cvelbar *J. Appl. Phys.* **2015**, *117*(4), 043304.

27. O. Baranov, G. Filipič, U. Cvelbar *Plasma Sources Sci. Technol.* **2019**, *28*(8), 084002.
28. A. Altaweel, T. Gries, S. Migot, P. Boulet, A. Mézin, T. Belmonte *Surf. Coatings Technol.* **2016**, *305*, 254.
29. A. Dey, G. Chandrabose, L. A. O. Damptey, E. S. Erakulan, R. Thapa, S. Zhuk, G. K. Dalapati, S. Ramakrishna, N. S. J. Braithwaite, A. Shirzadi, S. Krishnamurthy *Appl. Surf. Sci.* **2021**, *541*(1 March 2021), 148571.
30. A. Dey, P. Ghosh, J. Bowen, N. S. J. Braithwaite, S. Krishnamurthy *Phys. Chem. Chem. Phys.* **2020**, *22*(15), 7685.
31. M. Laroussi, T. Akan *Plasma Process. Polym.* **2007**, *4*(9), 777.
32. A. Dey, A. Chroneos, N. S. J. Braithwaite, R. P. Gandhiraman, S. Krishnamurthy *Appl. Phys. Rev.* **2016**, *3*(2), 021301.
33. J. Golda, J. Held, B. Redeker, M. Konkowski, P. Beijer, A. Sobota, G. Kroesen, N. S. J. Braithwaite, S. Reuter, M. M. Turner, T. Gans, O'D. Connell, V. Schulz-Von Der Gathen *J. Phys. D. Appl. Phys.* **2016**, *49*(8), 084003.
34. Y. Wu, P. Yang **2001**, *No. 22*, 3165.
35. *Appl. Phys. Lett.* **1964**, *4*(5), 89.
36. Y. Wang, S. Lany, J. Ghanbaja, Y. Fagot-Revurat, Y. P. Chen, F. Soldera, D. Horwat, F. Mücklich, J. F. Pierson *Phys. Rev. B* **2016**, *94*(24), 1.
37. U. Roland, F. Holzer, F. D. Kopinke In *Catalysis Today*, Elsevier, **2002**, Vol. *73*, pp 315.
38. X. Q. Deng, B. Zhu, X. S. Li, J. L. Liu, X. Zhu, A. M. Zhu *Appl. Catal. B Environ.* **2016**, *188*, 48.
39. K. Bazaka, O. Baranov, U. Cvelbar, B. Podgornik, Y. Wang, S. Huang, L. Xu, J. W. M. Lim, I. Levchenko, S. Xu *Nanoscale* **2018**, *10* (37), 17494.
40. L. Tian, H. Nie, N. P. Chatterton, C. J. Branford-White, Y. Qiu, L. Zhu *Appl. Surf. Sci.* **2011**, *257*(16), 7113.
41. J. Wu, K. Yin, M. Li, Z. Wu, S. Xiao, H. Wang, J. A. Duan, J. He *Nanoscale* **2020**, *12*(6), 4077.
42. F. Z. Zhang, R. A. Winholtz, W. J. Black, M. R. Wilson, H. Taub, H. B. Ma *J. Heat Transfer* **2016**, *138*(6).
43. H. Zhang, L. Li, B. Jiang, Q. Zhang, J. Ma, D. Tang, Y. Song *ACS Appl. Mater. Interfaces* **2020**, *12*(14), 16503.
44. S. Olveira, A. Stojanovic, S. Seeger In *Functional Polymer Coatings*, John Wiley & Sons, Inc: Hoboken, NJ, **2015**, pp 96.
45. A. Roy, H. S. Jadhav, M. Cho, J. G. Seo *J. Ind. Eng. Chem.* **2019**, *76*, 515.
46. Y. Deng, A. D. Handoko, Y. Du, S. Xi, B. S. Yeo *ACS Catal.* **2016**, *6*(4), 2473.
47. A. Dey, A. Lopez, G. Filipič, A. Jayan, D. Nordlund, J. Koehne, S. Krishnamurthy, R. P. Gandhiraman, M Meyyappan. *J. Vac. Sci. Technol. B* **2019**, *37*(3), 031203.
48. A. Dey, S. Krishnamurthy, J. Bowen, D. Nordlund, M. Meyyappan, R. P. Gandhiraman *ACS Nano* **2018**, *12*, 5473.
49. M. C. Biesinger, L. W. M. Lau, A. R. Gerson, R. S. C. Smart *Appl. Surf. Sci.* **2010**, *257*(3), 887.
50. Z. Wang, L. Zhang, T. U. Schülli, Y. Bai, S. A. Monny, A. Du, L. Wang *Angew. Chemie* **2019**, *131*(49), 17768.
51. L. Tao, Y. Shi, Y. C. Huang, R. Chen, Y. Zhang, J. Huo, Y. Zou, G. Yu, J. Luo, C. L. Dong, S. Wang *Nano Energy* **2018**, *53*(August), 604.
52. M. M. Besli, C. Usubelli, M. Metzger, V. Pande, K. Harry, D. Nordlund, S. Sainio, J. Christensen, M. M. Doeff, S. Kuppan *ACS Appl. Mater. Interfaces* **2020**, *12*(18), 20605.
53. A. Sharma, M. Varshney, J. Park, T. K. Ha, K. H. Chae, H. J. Shin *RSC Adv.* **2015**, *5*(28), 21762.
54. S. T. Hartman, B. Mundet, J. C. Idrobo, X. Obradors, T. Puig, J. Gázquez, R. Mishra *Phys. Rev. Mater.* **2019**, *3*(11), 1.
55. X. Sun, W. Zhu, D. Wu, Z. Liu, X. Chen, L. Yuan, G. Wang, R. Sharma, G. Zhou *Adv. Funct. Mater.* **2020**, *30*(4), 1.
56. G. Modi, E. A. Stach, R. Agarwal *ACS Nano* **2020**, *14*(2), 2162.
57. X. Liu, S. Cui, Z. Sun, Y. Ren, X. Zhang, P. Du *J. Phys. Chem. C* **2016**, *120*(2), 831.
58. S. M. Pawar, J. Kim, A. I. Inamdar, H. Woo, Y. Jo, B. S. Pawar, S. Cho, H. Kim, H. Im *Sci. Rep.* **2016**, *6*(1), 1.
59. Y. Sun, Y. Zhou, C. Zhu, W. Tu, H. Wang, H. Huang, Y. Liu, M. Shao, J. Zhong, S. T. Lee, Z Kang. *Appl. Catal. B Environ.* **2019**, *244*(November 2018), 795.
60. N. G. Schmahl, G. F. Eikerling *Zeitschrift fur Phys. Chemie* **1968**, *62*(5–6), 268.
61. B. Himmetoglu, R. M. Wentzcovitch, M. Cococcioni *Phys. Rev. B - Condens. Matter Mater. Phys.* **2011**, *84*(11), 115108.
62. R. F. W. Bader *Theor. Chem. Acc.* **2001**, *105*(4–5), 276.
63. H. Yu, J. Yu, S. Liu, S. Mann *Chem. Mater.* **2007**, *19*(17), 4327.
64. T. S. Natarajan, H. C. Bajaj, R. J. Tayade *J. Colloid Interface Sci.* **2014**, *433*, 104.
65. H. Li, Z. Su, S. Hu, Y. Yan *Appl. Catal. B Environ.* **2017**, *207*, 134.
66. C. Feng, Z. Chen, J. Jing, J. Hou *J. Mater. Chem. C* **2020**, *8*(9), 3000.
67. L. Wang, Z. Bian *Chemosphere* **2020**, *239*, 124815.
68. E. Moctezuma, E. Leyva, C. A. Aguilar, R. A. Luna, C. Montalvo *J. Hazard. Mater.* **2012**, *243*, 130.

SUPPORTING INFORMATION

Additional supporting information may be found online in the Supporting Information section at the end of the article.

How to cite this article: A. Dey, P. Ghosh, G. Chandrabose, L. A. O. Damptey, N. Kuganathan, S. Sainio, D. Nordlund, V. Selvaraj, A. Chroneos, N. St J. Braithwaite, S. Krishnamurthy. *Nano Select*. **2021**, 1. https://doi.org/10.1002/nano.202100191